RSC Advances

PAPER

View Article Online
View Journal | View Issue

Cite this: *RSC Adv.*, 2022, **12**, 12552

$BiVO_4/Fe_2O_3/ZnFe_2O_4$; triple heterojunction for an enhanced PEC performance for hydrogen generation†

Sakshi Saxena,[a] Anuradha Verma,[a] Kumari Asha,[a] Neeraj Kumar Biswas,[a] Anupam Srivastav,[a] Vibha Rani Satsangi,[b] Rohit Shrivastav[a] and Sahab Dass *[a]

Received 11th February 2022
Accepted 3rd April 2022

DOI: 10.1039/d2ra00900e

rsc.li/rsc-advances

n/n/n triple heterojunction photoanodes made up of Zr:W-$BiVO_4$, Fe_2O_3, and $ZnFe_2O_4$ metal oxides are fabricated through a simplistic spray pyrolysis method. Use of Zr and W as dopants in $BiVO_4$ plays an important role as Zr increases the carrier density and W reduces the charge recombination. Further, Fe_2O_3 and $ZnFe_2O_4$ serve as a protective layer for Zr:W-$BiVO_4$, which augmented the photoelectrochemical performance and achieved a 1.90% conversion efficiency in the triple heterojunction. XRD measurements display the crystalline nature and reduction in particle size due to strain in the sample, UV-vis absorbance shows an extended absorption towards the visible region and the FE-SEM imaging confirms the successful deposition of $ZnFe_2O_4$ over $BiVO_4/Fe_2O_3$. By analyzing the band edge position, it was observed that on formation, the triple heterojunction not only suppresses the charge carrier recombination but also utilizes the band edge offset for the water splitting reaction using solar energy.

1. Introduction

India, which is the most polluted and largest economic country in the world, demands a speedy adaptation of energy from carbon-based fossil fuels to renewable energy sources with zero carbon emission to accomplish the target of 450 GW of renewable energy by the year 2030. In this transformation procedure, photoelectrochemical (PEC) water splitting utilizing solar energy-absorbing semiconductors for the production of green fuel hydrogen arises as a growing technique.[1–4] Among different semiconductors, metal oxide semiconductors have gained attention due to their economical nature and stability as compared with that of other non-oxide semiconductors.[5] $BiVO_4$ and Fe_2O_3 with low bandgaps (1.8–2.2 eV) show good stability in the alkaline medium and are non-toxic and cost-effective materials. These are considered as excellent candidates for the oxidation reaction, but some limitations, such as the recombination of the electron–hole, smaller diffusion length, deprived electrical conductivity, *etc.*, restrict their application as photoanodes.[5–12] Recently, closed packed $A^{II}B^{III}O_4$ type spinel materials, *viz.* n-type zinc ferrite ($ZnFe_2O_4$), have gained inclusive curiosity as promising candidates for photoelectrochemical accomplishments as well as photocatalytic activities due to their distinctive properties, *viz.* a small bandgap (1.9 eV) for exploiting maximum visible light, brilliant photoelectrochemical stability in a basic medium, economical, nontoxic, environment and eco-friendly.[13–19] However, the speedy recombination of charge carriers and low valence band potential are the major limitations of $ZnFe_2O_4$ in the field of photoelectrochemical studies.[5,15,16] Their photoelectrochemical properties mostly depend upon morphology, chemical composition, and crystal size, which can be upgraded by introducing several alteration procedures, such as doping/co-doping, building a heterojunction system, use of co-catalyst, *etc.*[10,20–22] Among these, heterojunction formation is considered as an excellent way to overcome the limitations of metal oxides due to its several advantages, *viz.* enhanced separation, reduced recombination of charge carriers, and extended absorption in the visible region.[11,15,23,24]

In this report, we fabricated a novel type-II heterojunction Zr-W:$BiVO_4/Fe_2O_3/ZnFe_2O_4$ by a facile spray pyrolysis method. We have previously reported the fabrication of co-doped (Zr, W) bismuth vanadate films, and a maximum photoresponse of 0.13 mA cm^{-2} at 1.23 V/RHE was obtained with 3.5% Zr and 4% W dopant concentrations. In the present work, the deposition of Fe_2O_3 and $ZnFe_2O_4$ over the best performing Zr,W co-doped $BiVO_4$ was expected to achieve the best PEC performance. The as-prepared type-II n/n/n triple heterojunction exhibited the superior PEC performance. The advantage of constructing this heterojunction falls on the following points: (i) comparable energy level of Fe_2O_3 over $BiVO_4$; especially, the VB positions of

[a]*Department of Chemistry, Dayalbagh Educational Institute, Dayalbagh, Agra 282005, India. E-mail: drsahabdas@gmail.com*

[b]*Department of Physics and Computer Science, Dayalbagh Educational Institute, Dayalbagh, Agra 282005, India*

† Electronic supplementary information (ESI) available. See https://doi.org/10.1039/d2ra00900e

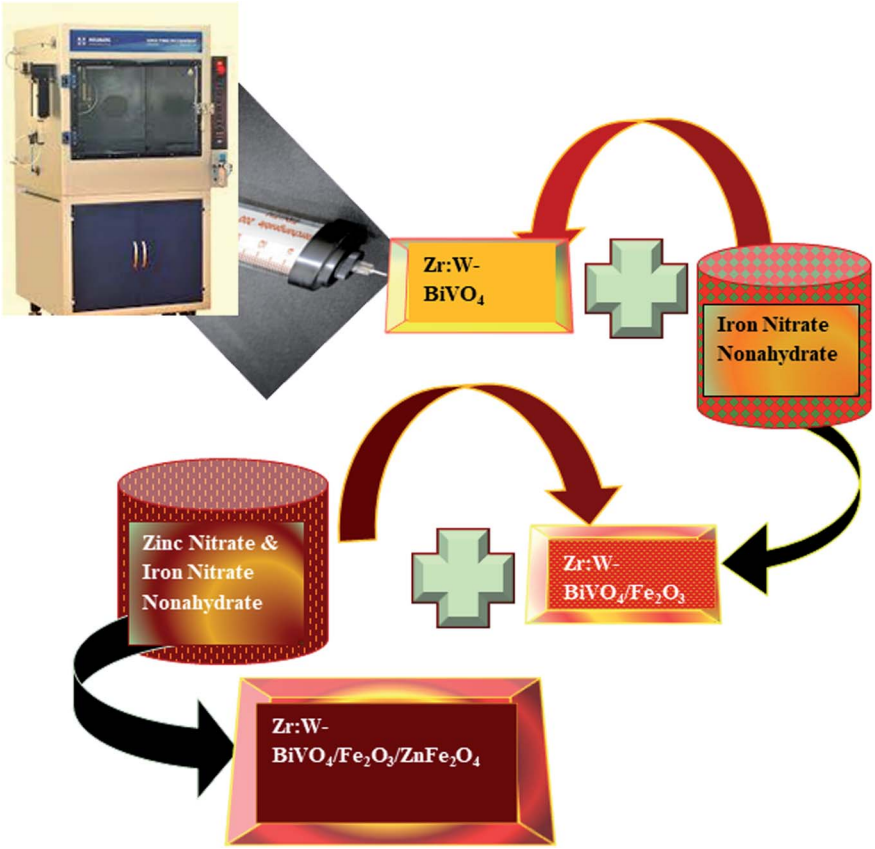

Fig. 1 Schematic representation showing the preparation of the Zr:W-$BiVO_4/Fe_2O_3/ZnFe_2O_4$ heterojunction thin film.

Fe_2O_3 are more suitable for constructing a type-II heterojunction for a hole transfer reaction (a high-performance $BiVO_4$ photoanode co-catalyzed with an ultrathin Fe_2O_3 layer for PEC application), (ii) similarly, the benefit of $ZnFe_2O_4$ over Fe_2O_3 lies in the straddling conduction band maxima position, as shown in Fig. 9(a), because the CB of $ZnFe_2O_4$ is more negative than that of Fe_2O_3.[25,26] Hence, constructing Zr-W:$BiVO_4/Fe_2O_3/ZnFe_2O_4$ for the first time could effectively utilize the band edge offset for a water-splitting reaction using solar energy.

2. Experimental section

2.1. Preparation of the triple heterojunction Zr-W:$BiVO_4/Fe_2O_3/ZnFe_2O_4$ photoanode

The preparation of Zr:W-$BiVO_4/Fe_2O_3/ZnFe_2O_4$ heterojunction thin films was completed in three steps. In the first step, Zr:W-$BiVO_4$ thin films were prepared (the details of fabrication already reported by the authors, see ref. 29). In the second step, Fe_2O_3 thin films were prepared with a calculated amount of iron nitrate nonahydrate, which dissolved in DM water and deposited over Zr:W-$BiVO_4$ at a flow rate of 500 μL min^{-1} at 250 °C temperature maintained over a hot plate. Finally, the films were annealed at a temperature of 450 °C for 2 h (the resulting thin films appear brown) to forms a double heterojunction, Zr:W-$BiVO_4$ (symbolized as BF in the manuscript). In the last step, zinc ferrite thin films were prepared with a 1 : 2 ratio of zinc(II) nitrate hexahydrate and ferric nitrate nonahydrate mixed in DM water and deposited over the Zr-W:$BiVO_4/Fe_2O_3$ thin films at a temperature of 250 °C to obtain the Zr-W:$BiVO_4/Fe_2O_3/ZnFe_2O_4$ thin films (symbolized as BFZ) using a spray pyrolysis method (as shown in Fig. 1). Pristine $ZnFe_2O_4$ thin films were also prepared with the spray pyrolysis method at a 500 μL min^{-1} flow rate at 250 °C temperature.[11,27–29] A detailed description of the prepared thin films is given in Table 1.

2.2. Characterizations

2.2.1. General characterizations. XRD patterns of the prepared triple heterojunction thin films were recorded with a Bruker AXS D-8 Advance X-ray diffractometer with a Cu-Kα source having a wavelength of 1.54 Å. XRD data were further

Table 1 Acronyms and description of the prepared thin films

Sample	Acronym
(3.5% Zr + 4% W-$BiVO_4$)	B
Fe_2O_3	F
$ZnFe_2O_4$	Z
(3.5% Zr + 4% W-$BiVO_4$) + Fe_2O_3	BF
(3.5% Zr + 4% W-$BiVO_4$) + $ZnFe_2O_4$	BZ
Fe_2O_3 + $ZnFe_2O_4$	FZ
(3.5% Zr + 4% W-$BiVO_4$) + Fe_2O_3 + $ZnFe_2O_4$	BFZ

used to calculate the particle size using the Debye–Scherrer's equation.[23,27] Field Emission Scanning Electron Microscopy (FE-SEM) using a JEOL, JSM 7610 F Plus system in connection with Oxford Energy Dispersive X-ray Spectroscopy (EDX) was employed for the morphology and compositional analysis. Further, the elemental composition was confirmed using X-ray photoelectron spectroscopy (PHI 5000 versa Probe II, FEI Inc.) equipped with a C60 sputter gun and Mg-Kα radiation with Ar ion. The absorbance–wavelength spectrum was recorded using a double beam UV-visible spectrophotometer (UV-2450, Shimadzu, Japan) in the 400–800 wavelength range and absorbance data were utilized for bandgap calculation using the Tauc plot.[23,29,30]

2.2.2. Photoelectrochemical and electrochemical characterizations. Photoelectrochemical (PEC) and electrochemical characterizations of the prepared heterojunction thin films were recorded using an electrochemical workstation (EWS, Model: PP211, CIMPS-pcs, Zahner, Germany), through back-side illumination. A typical PEC cell consists of a saturated calomel electrode (SCE) as reference electrode, Pt electrode as a counter electrode, and a triple heterojunction photoanode as a working electrode dipped in 0.1 M NaOH solution at pH 13 was used for the PEC measurements. An area of 1×1 cm^2 was exposed using a 150 W xenon arc lamp with 100 mW cm^{-2} light intensity.

The photocurrent data obtained from the current–potential analysis were used to calculate the applied bias photon to current conversion efficiency (ABPE) using eqn (1).

$$\text{ABPE}\ (\%) = J_{\text{ph}}\ (\text{mA cm}^{-2})\{1.23 - V_{\text{b}}\ (\text{V})\}/P_{\text{Total}}\ (\text{mW cm}^{-2}) \quad (1)$$

where J_{ph} = photocurrent density, P = illumination intensity, $V_{\text{b}} = V_{\text{meas}} - V_{\text{oc}}$ (V_{meas} = photovoltage at which the photocurrent was measured, V_{oc} = open circuit potential). Mott–Schottky experiments were performed to find the flat band potential and charge carrier density (N_{d}). The intercept of the $1/C^2$ *vs.* the applied bias graph gives the value of the flat band potential (eqn (2)) while N_{d} was calculated using eqn (3):[11,12]

$$\frac{1}{C^2} = \frac{2}{q\varepsilon\varepsilon_{\text{o}}N_{\text{d}}}\left(V_{\text{app}} - V_{\text{FB}} - \frac{KT}{q}\right) \quad (2)$$

$$S = 2/\varepsilon\varepsilon_{\text{o}}qN_{\text{d}} \quad (3)$$

where, q is the electronic charge, ε and ε_{o} are the permittivities of the semiconductor and vacuum, respectively, S is the slope, N_{d} is the donor density, V_{app} is the applied potential and V_{FB} is the flat band potential. The electrochemical surface area (ECSA) was also calculated using cyclic voltammetry under dark conditions and at different scan rates. The Nyquist analysis was executed with electrochemical impedance spectroscopy (EIS) to obtain the charge transfer kinetics at a 5 mV amplitude and in

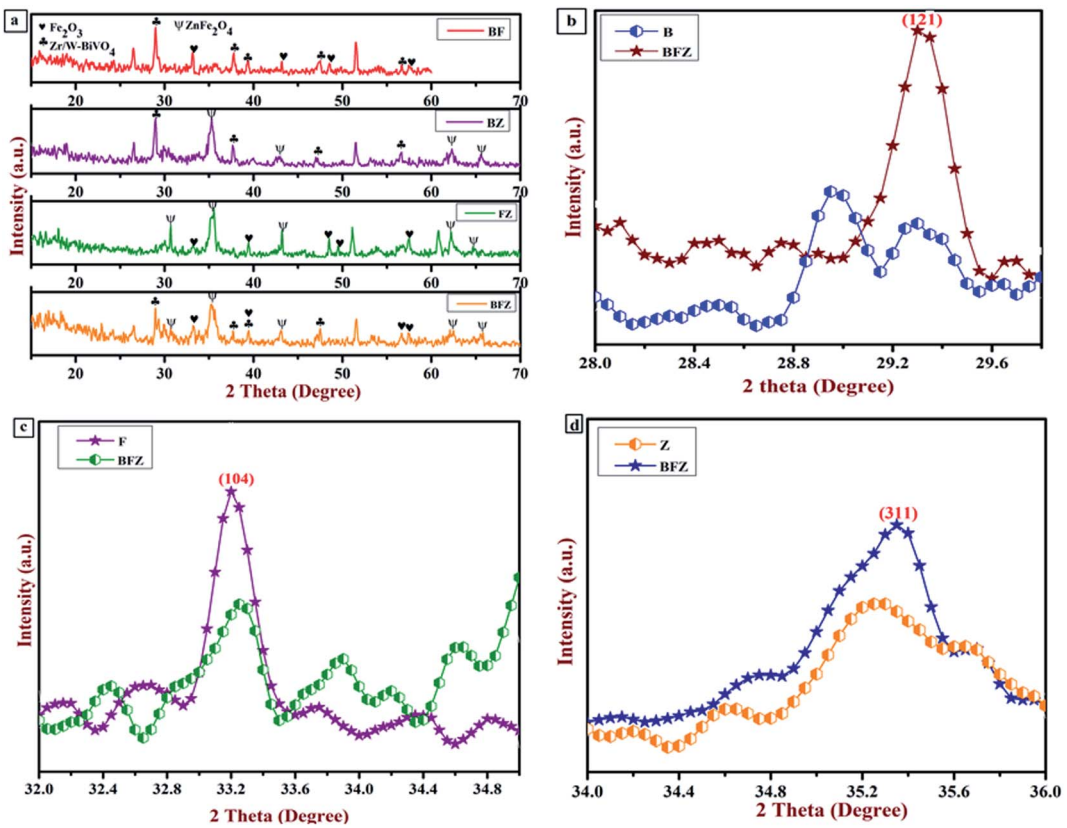

Fig. 2 (a) XRD patterns of all the prepared thin films; (b) enlarged image of the highest intensity peaks of the B and BFZ samples; (c) enlarged image of highest intensity peaks of F and BFZ; (d) enlarged image of highest intensity peaks of Z and BFZ.

the frequency range of 100 MHz to 10 kHz. This analysis was performed under dark conditions.

3. Results and discussion

3.1. Crystal structure analysis: XRD spectrum

The crystal structure analysis was obtained from the XRD instrument. Fig. 2(a–d) displays the XRD patterns of Zr:W-$BiVO_4/Fe_2O_3/ZnFe_2O_4$ (BFZ), Zr:W-$BiVO_4/Fe_2O_3$ (BF), $Fe_2O_3/ZnFe_2O_4$ (FZ), Zr:W-$BiVO_4/ZnFe_2O_4$ (BZ) along with Fe_2O_3 (F) and $ZnFe_2O_4$ (Z) which exhibited the polycrystalline nature of the prepared thin films. The diffraction peaks at 28.9° (121), 37.8° (220), 39.4° ($\overline{1}14$), and 47.54° (042) corresponds to the scheelite monoclinic phase of $BiVO_4$ (JCPDS card no. 140688) while peaks at 33.1° (104), 35.6° (110), 39.4° (006), 43.5° (202), and 56.7° (211) confirm the presence of rhombohedral α-Fe_2O_3 (JCPDS card no. 1890599) over the Zr:W-$BiVO_4$ which matches with the literature reported values.[29–31] In addition to this, the 2 theta peaks in the BFZ thin film at 29.9° (220), 35.3° (311), 43.1° (400), 46.8° (331), 62.6° (440), and 65.6° (531) confirms the formation of cubic $ZnFe_2O_4$ (JCPDS card no. 821042) over the Zr:W-$BiVO_4/Fe_2O_3$ thin films.[32,33] These XRD patterns with the existence of the highest intensity peaks of Zr:W-$BiVO_4$ (B) at 28.9°, Fe_2O_3 (F) at 33.1°, and $ZnFe_2O_4$ (Z) at 35.3° approve the formation of the BFZ heterojunction. A higher angle shift in the highest intensity peak of BFZ in comparison with those of B, F, and Z was observed, which proposes strain in the sample (as shown in Fig. 2(b–d)).[30]

Table 2 Variation in particle size in different samples

	Particle size (nm)			Lattice strain		
Sample	B	F	Z	B	F	Z
BFZ	**27.48**	**27.07**	**10.12**	**0.0053**	**0.0047**	**0.0118**
BZ	31.4	—	14.03	0.0048	—	0.0085
FZ	—	28.31	14.08	—	0.0045	0.0085
F	—	39.73	—	—	0.0032	—
Z	—	—	20.88	—	—	0.0057

Further, the average crystallite size was also determined by Debye–Scherrer's equation and it was observed that particle size decreases in the heterojunction system in comparison with that of the other sample, which confirms the presence of lattice strain in the sample. Table 2 shows the variation in particle size in different samples.

3.2. Optical analysis: UV-visible absorption spectrum

Absorbance–wavelength spectra of the prepared thin films were investigated through a UV-vis spectrophotometer. Fig. 3(a) shows the absorption spectrum of all the thin films in the wavelength range of 300–800 nm. From Fig. 3(a), it is clear that heterojunction (BFZ) shows a prominent absorption edge at around 660 nm in comparison with those of the other samples which indicates that the sample has a strong tendency to engross a maximum number of photons and produce more charge carriers. Further, the optical band gap of all the prepared thin films was calculated using the Tauc plot, as shown in Fig. 3(b). The pristine Zr:W-$BiVO_4$ (B) has a bandgap of 2.16 eV as shown in Fig. S1 (ESI†) while the bandgaps for F, Z, and BFZ are 2.16 eV, 2.15 eV, 2.07 eV, and 1.99 eV, respectively, confirms that the heterojunction sample demonstrated a good photo-activity in comparison with those of other samples.[29,33] Table 3 shows the bandgap values of all the samples.

3.3. Elemental valency and chemical compositional analysis: XPS spectra

XPS analysis was executed to examine the chemical composition and valency of each element present in the sample. Fig. 4 shows the XPS spectrum of the Zr:W-$BiVO_4/Fe_2O_3/ZnFe_2O_4$ (BFZ) thin film. The full scan survey (Fig. 4(a)) confirms the presence of Bi, V, Zr, W, Fe, Zn, and O as the major elements while the peak at 285.2 eV is ascribed to the standard peak of a carbon atom. The presence of Bi as Bi^{3+}, V as V^{5+}, W as W^{6+} and Zr as Zr^{4+} was confirmed from previous work.[29,34] The peak at 708.5 eV and 723.5 eV, as shown in Fig. 4(b), correspond to Fe $2p_{1/2}$ and $2p_{3/2}$, while a small satellite peak at 714.5 eV confirms the presence of Fe in the sample with a trivalent state.[9,31,35] The Zn 2p XPS spectrum (Fig. 4(c)) exhibits two peaks at 1018.7 eV and

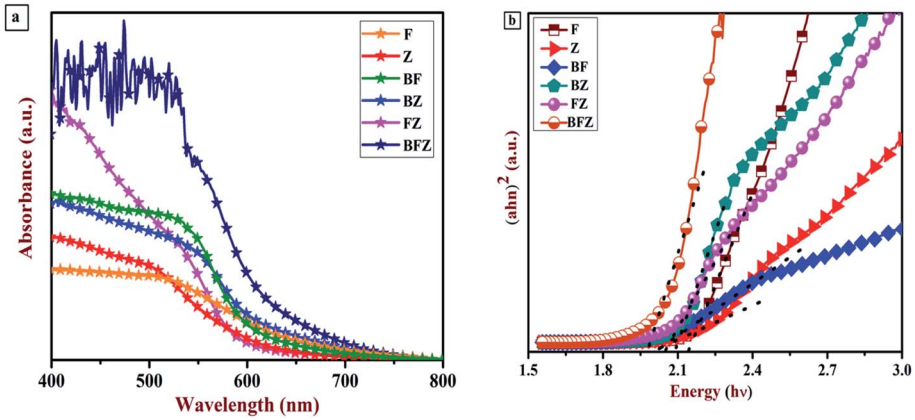

Fig. 3 (a) UV-visible absorption spectrum of all the prepared thin films (b) Tauc plot of all the prepared thin films.

Table 3 Calculated band gap values

Sample	Band gap (eV)
B	2.16
F	2.10
Z	1.92
BF	2.01
BZ	2.04
FZ	2.03
BFZ	1.99

1041.9 eV, which resemble those of Zn $2p_{3/2}$ and $2p_{1/2}$. The presence of these two peaks confirms that Zn is present in the divalent state.[36–39] The O 1s spectrum has two peaks at 527.2 eV and 528.8 eV, which correspond to the lattice oxygen and hydroxyl group as shown in Fig. 4(d). A shift in the peaks from the peak positions reported in the literature (*i.e.* in the case of Zn, 1018 eV and 1041 eV instead of 1022.1 and 1045.2 eV; in the case of O, 527 eV and 528 eV instead of 529.5 and 530.9 eV; and in the case of Fe, 723 eV and 708 eV instead of 725.2 and 711.1 eV) confirms the chemical interaction between the elements of $BiVO_4$, $ZnFe_2O_4$, and Fe_2O_3, which reaffirms the formation of $Fe_2O_3/ZnFe_2O_4$ over the $BiVO_4$.[31]

3.4. Morphological analysis

A morphological analysis of all the prepared thin films was executed with a JSM-7610F Field Emission Scanning Electron Microscope and the corresponding SEM images are shown in Fig. 5(a–f). A uniform and compactly grown morphology was seen in the case of BF, BZ, F, and BFZ. Spherical, round and elongated shape particles with a porous network uniformly grown over the substrate are observed in Fig. 5(d–f). The best performing triple heterojunction system (Zr:W-$BiVO_4/Fe_2O_3/ZnFe_2O_4$) shows a root mean square (RMS) roughness of 1.51 nm, which is the highest in comparison to those of all the other samples and therefore favors a high photoelectrochemical activity (as shown in Table 4).

Further, EDX (Energy Dispersive X-ray Spectroscopy) analysis was also performed to confirm the elements present in the triple heterojunction thin-film BFZ. The cross-SEM image (Fig. 6(a)) of the thin film was scanned for EDX analysis from the bottom to the top direction (from B to Z) and their corresponding graphs are shown in Fig. 6(a–c). From Fig. 6(a and b) it is clear that all the elements, such as Zr, W, Bi, V, O, Fe and Zn are present in the sample and confirm the formation of heterojunction system. From Fig. 6(c) it is clear that the line scan carried out in the bottom to top direction shows that initially the amount of Bi and V increases and then decreases, which confirms that $BiVO_4$ is present as the bottom layer and Fe is increasing towards the

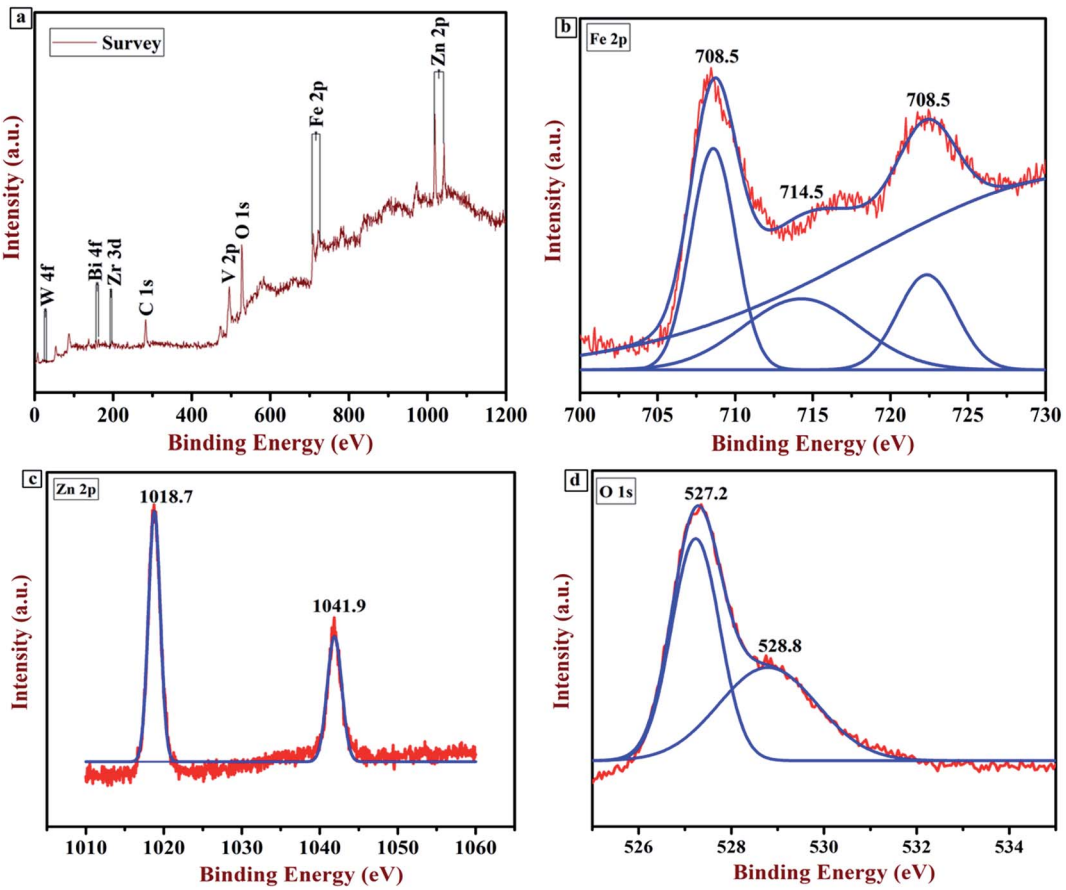

Fig. 4 (a) Full scan survey of the Zr:W-$BiVO_4/Fe_2O_3/ZnFe_2O_4$ thin film; (b) XPS spectrum of the Fe 2p element; (c) XPS spectrum of the Zn 2p element; (d) XPS spectrum of the O 1s element.

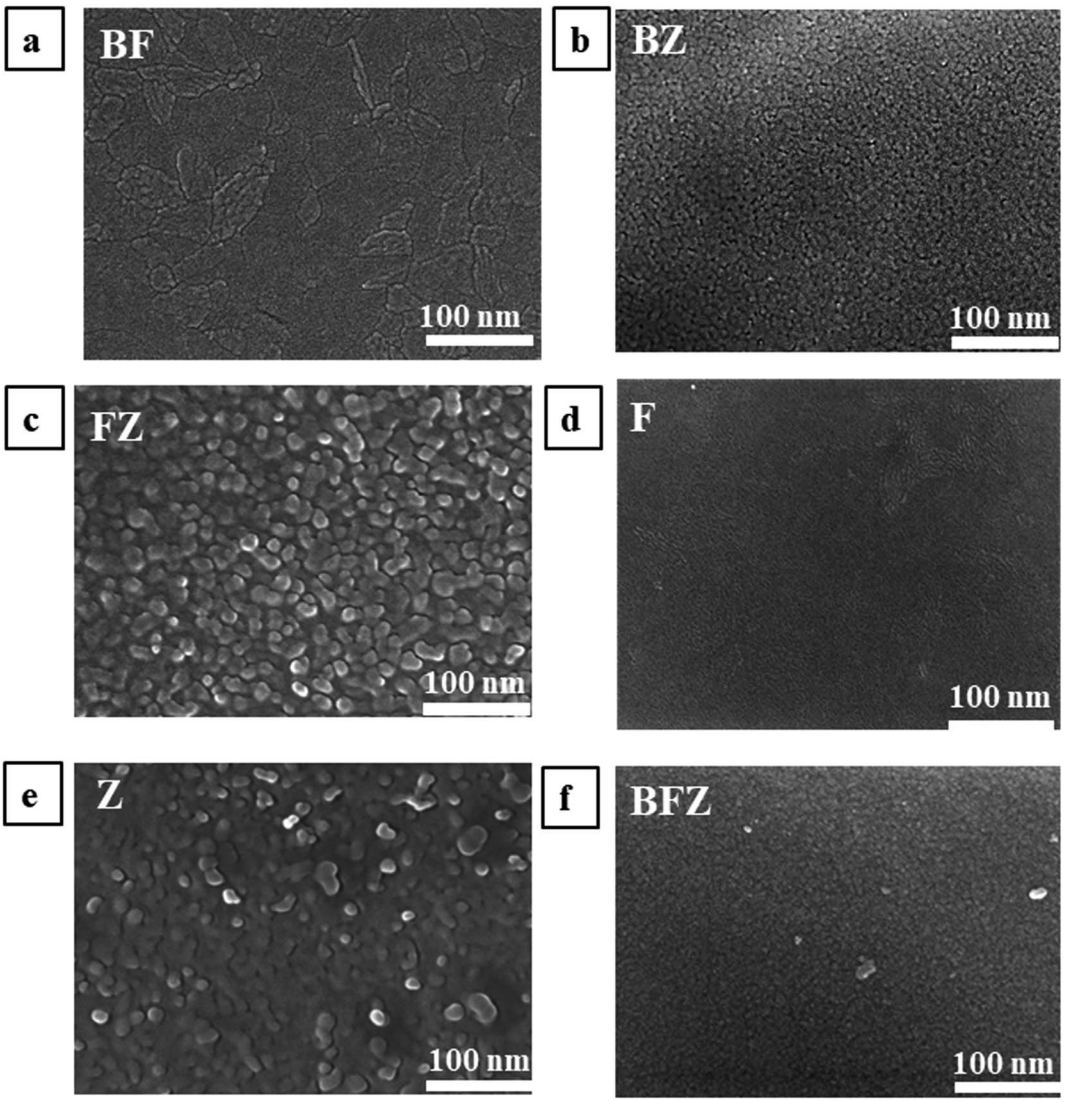

Fig. 5 (a–f) FESEM images of all the prepared thin films taken at 100 nm.

Table 4 RMS value of all the prepared thin films

Sample	RMS roughness (nm)
F	1.31
Z	1.16
BF	1.22
BZ	1.39
FZ	1.31
BFZ	1.51

top layer, confirming its presence in the middle layer of Fe_2O_3 and top layer of $ZnFe_2O_4$. The amount of O was almost constant, which confirms that O is present throughout the sample.

3.5. Photoelectrochemical analysis: current–voltage graph

The most valuable indicator for the PEC water splitting process is the conversion efficiency and linear sweep voltammetry (LSV).[40] These two factors were recorded to explain the current–voltage characteristic and ABPE efficiency using three-electrode cells in a suitable electrolyte under AM 1.5G illumination. Fig. 7(a, b) and S2 (ESI†) show the current–voltage graphs (attained through linear sweep voltammetry and transient analysis) for all the prepared thin films in the potential range of −0.5 V to +1.0 V/SCE (0.5 to 2.0 V/RHE). The pristine sample here is Zr:W-$BiVO_4$ (B), which shows the photocurrent density (PCD) of 0.13 mA cm^{-2} at 1.23 V/RHE (S. Saxena *et al.* 2021;[29]), and this value increased to 1.85 mA cm^{-2} after the deposition of Fe_2O_3 (F) over the B thin films. In addition to this, when $ZnFe_2O_4$ (Z) was deposited over the BF thin films, the PCD enhanced to 2.47 mA cm^{-2} at 1.23 V/RHE which was nineteen and two times higher than those of the B and BF samples, respectively (shown in Fig. 7(a)). This augmentation in photo-response is due to the amended crystallinity and a properly staggered type of alignment of the B, F, and Z semiconductors. As a result, $ZnFe_2O_4$ (Z) transfers the electrons (generated

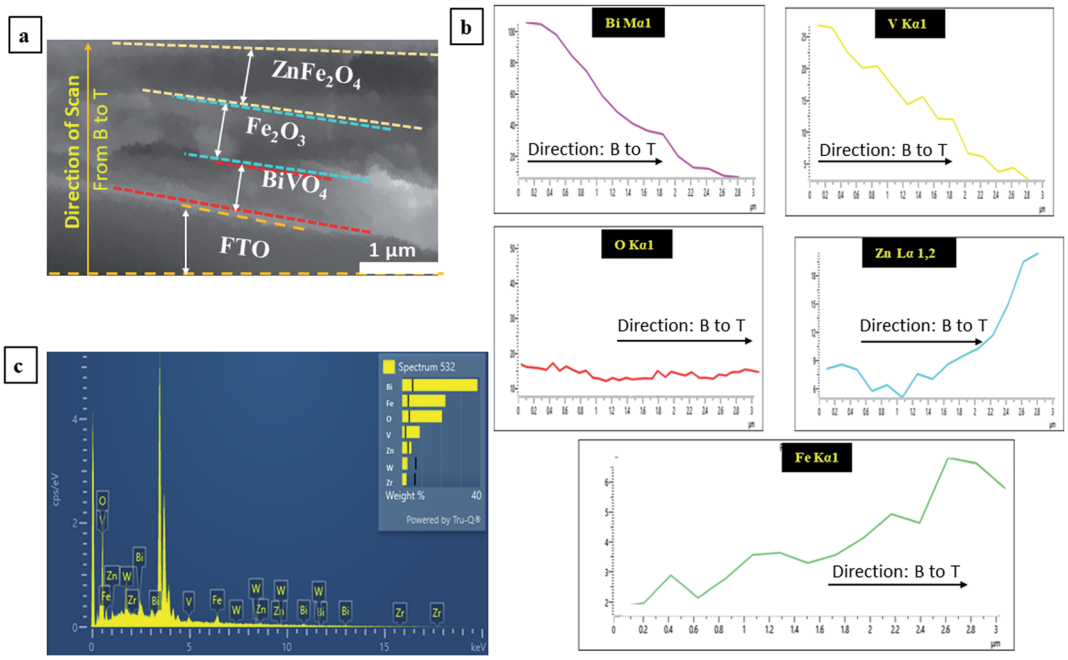

Fig. 6 (a) Cross SEM image of the triple heterojunction; (b and c) EDS analysis from Bottom (B) to Top (T) (from B to Z). Here: B: $BiVO_4$; F: Fe_2O_3; and Z: $ZnFe_2O_4$.

through water splitting) to the core of Fe_2O_3 (F) and then to Zr:W-$BiVO_4$ (B) which efficiently diminishes the recombination of photogenerated charge carriers and enhances the separation of electron–hole pairs as well as PEC performance. A chopped light study was performed in 0.1 M NaOH and the graphs are shown in Fig. 7(b). From Fig. 7(b) it is visible that the BFZ showed the minimum spikes and maximum PCD, which indicates that the sample possesses a lesser charge recombination.[11,21,25,29,31] Subsequently, photogenerated holes that reach the interface participate in the water oxidation reaction. Fig. 7(c) shows the ABPE plot of all the prepared thin films. From Fig. 7(c) it is clear that BFZ possesses a maximum ABPE of 1.90%, which indicates the least charge transfer resistance and an enhanced separation of the charge carriers. Table 5 shows the photoelectrochemical parameters of all the prepared thin films recorded in a 0.1 M NaOH electrolyte.

The stability of the best performing BFZ sample was executed in 0.1 M NaOH for 1 h (Fig. 7(d)). From Fig. 7(d) it is clear that the sample showed stability with an initial current of 7.99 mA, which decreased to 7.58 mA after continuous illumination. A graduated inverted tube was used to measure the evolution of gases (hydrogen and oxygen) using the water displacement method. The ratio of evolved H_2 to O_2 gas turns out to be 2 : 1, representing a faradaic efficiency of approximately unity (Fig. 7(e)).

3.6. Electrochemical analysis: Mott–Schottky and impedance analysis

Electrochemical analysis was accomplished under dark conditions using a three-electrode PEC setup to recognize the kinetics of the charge carriers across the heterojunction interface. Fig. 8(a) and S3 (ESI†) present the Mott–Schottky plots of all the prepared thin films. A Mott–Schottky plot between $1/C^2$ and the applied potential gives the value of the flat band potential (V_{FB}) and the nature of the prepared thin films. From Fig. 8(a), it is clear that heterojunction BFZ possesses a more negative value of the flat band potential in comparison with those of the other samples, which indicates a better separation of the photogenerated charge carriers across the interface. In addition to this, all the thin films display a positive slope that designates the n-type nature.[11,15,29,41] The flat band potential of the BFZ system is 0.39 eV/SCE which in magnitude is 0.11 eV, 0.02 eV, and 0.12 eV more negative than B, F, and Z, respectively. Further, the donor density of all the thin films was calculated and it was observed that donor density value of heterojunction BFZ is more in comparison to with those of the F and Z samples. The electrochemical active surface area (ECSA), which is involved in the water splitting reaction, was calculated from the cyclic voltammetry graphs and shown in Fig. S4 (ESI) and Table S1.† From Fig. S4(a–d) and Table S1,† it is clear that the surface area for the BFZ sample was 4.4 times and 3 times higher than those for the BZ and BF samples. This shows that BFZ exhibited efficient charge transfer kinetics at the interface.[39] Table 4 shows the flat band potential and donor density value of all the prepared thin films.

To examine the transfer kinetics of charge carriers at the interface, electrochemical impedance spectroscopic analysis was performed in which the Randles–Ershler model was applied as an equivalent circuit model on the obtained Nyquist plot, which gives information about the different types of resistance, as shown in Fig. 8(b) and S5 (ESI†). In the present study, an equivalent circuit was applied on the BFZ sample as shown in

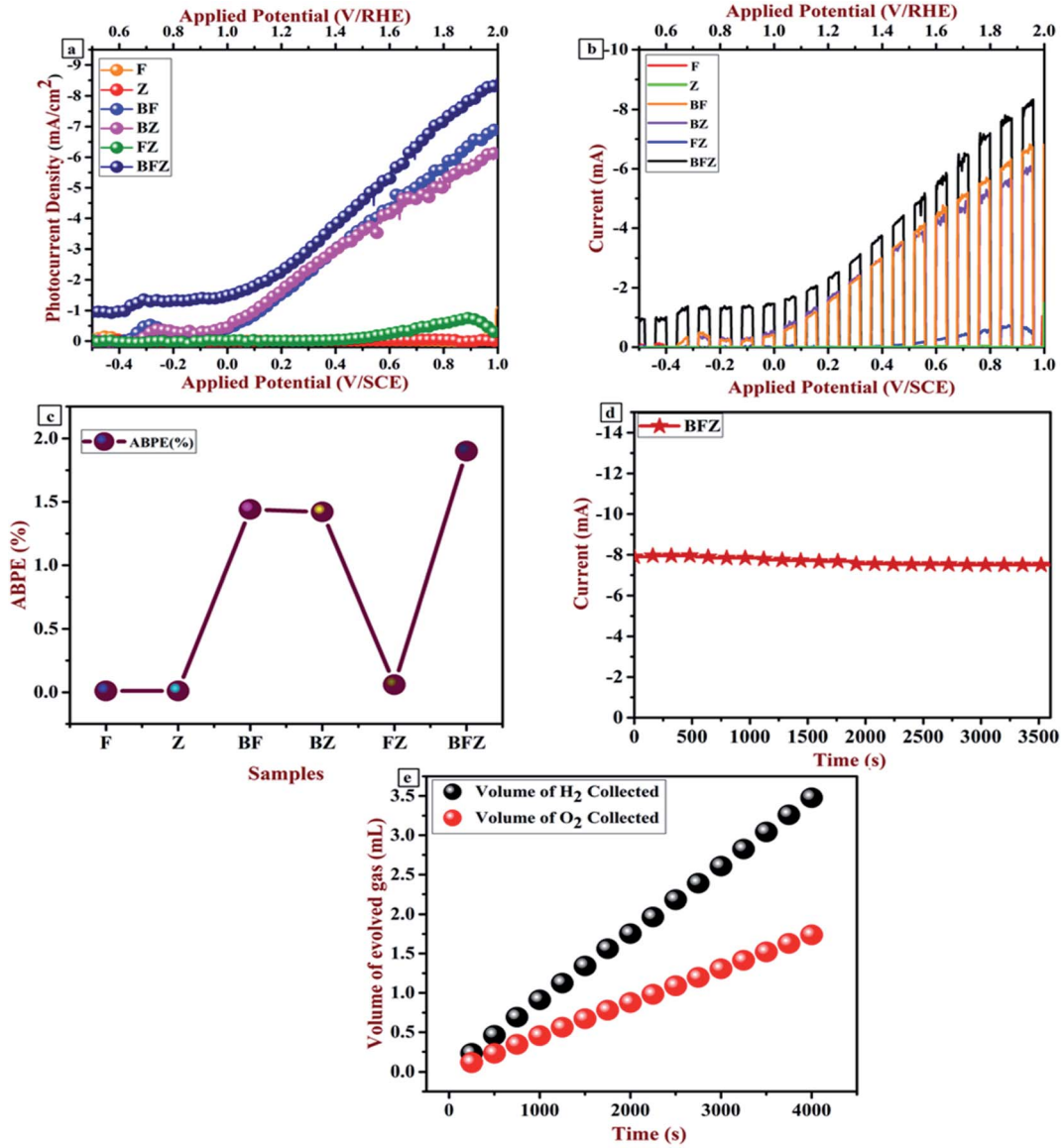

Fig. 7 (a and b) Current–voltage graph obtained through LSV and transient analysis; (c) ABPE graph; (d) chronoamperometric curve; (e) evolved hydrogen and oxygen measurement.

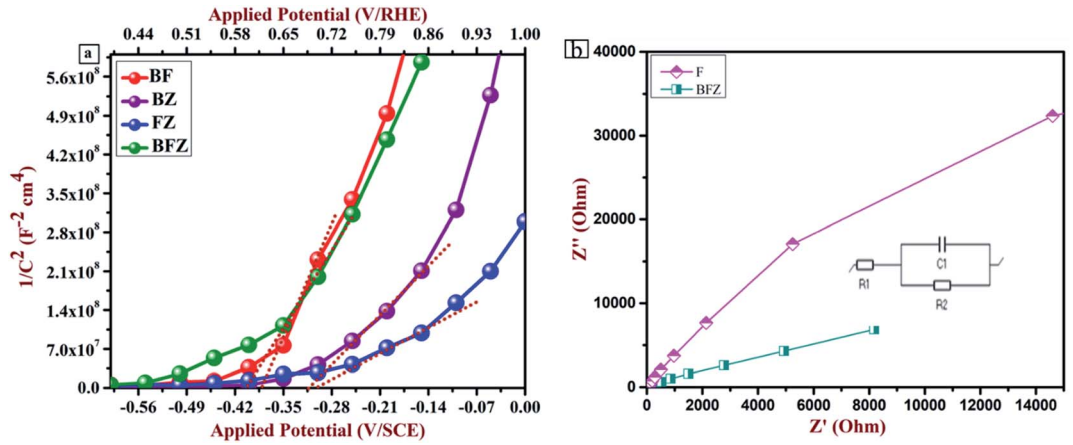

Fig. 8 (a) Mott–Schottky plot for all the prepared thin films (b) Nyquist plot for the F and BFZ thin films; (Inset) fitted equivalent circuit.

Table 5 Photoelectrochemical parameters of all the prepared thin films recorded in a 0.1 M NaOH electrolyte

Sample	PCD at 1.23 V/RHE (mA cm^{-2})	ABPE (%)	Flat band potential (V/SCE)	Donor density (cm^{-3})
B	0.13	0.05	0.28	4.0×10^{20}
F	0.01	0.01	0.37	3.2×10^{18}
Z	0.01	0.01	0.27	3.2×10^{18}
BF	1.85	1.44	0.37	7.7×10^{18}
BZ	1.85	1.42	0.31	4.2×10^{18}
FZ	0.08	0.06	0.29	4.0×10^{18}
BFZ	2.47	1.90	0.39	8.0×10^{18}

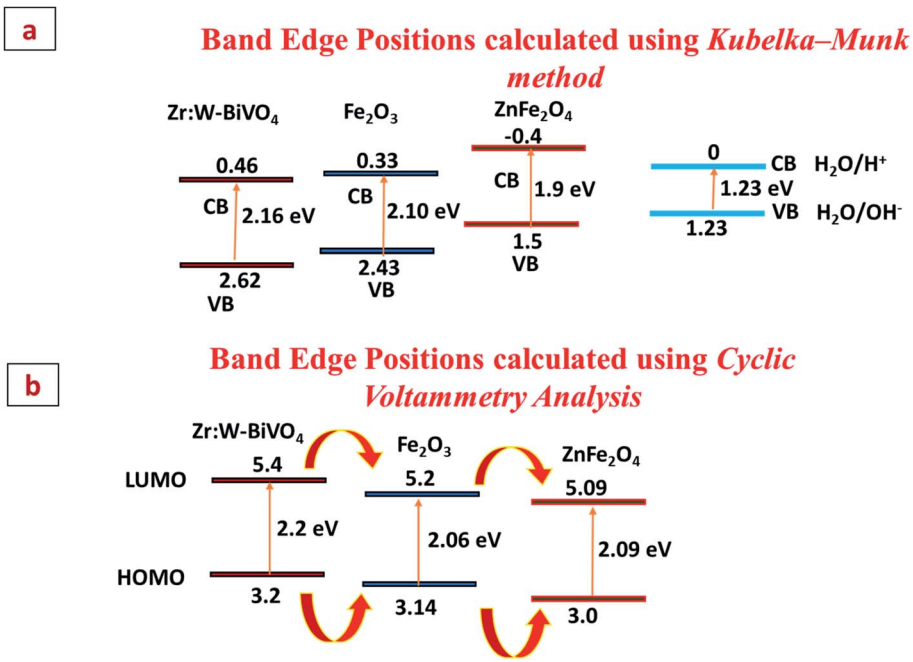

Fig. 9 (a and b) Band edge positions of B, F, and Z calculated using the Kubelka–Munk method and Cyclic Voltammetry Analysis.

Fig. 8(b) where two resistances, *i.e.*, solution resistance ($R1$) and charge transfer resistance ($R2$), and one capacitance ($C1$), were observed across the interface. Generally, the arc radius in the Nyquist plot is an indicator of an improved charge transfer across the interface and it was observed that heterojunction BFZ exhibited a smaller arc radius in the Nyquist plot in comparison with those the other samples under investigation. This was due to the proper staggered type-II band alignment, which promotes the charge transfer and separation at the interface.[42–44] The fitted values obtained from the equivalent circuit are shown in Table S2 (ESI†).

3.7. Mechanism of enhancement in PEC performance

The mechanism behind the improved PEC performance can be explained on the basis of the band edge positions of metal oxide semiconductors, which allow the transportation of electron and hole pairs. Two methods were adopted in order to calculate the band edge positions and then compare them with literature reported values. First is the Kubelka–Munk method in which the following equations were used to estimate the conduction band and valence band positions.

$$E_{CB} = X - E^{c} - 0.5E_{g}$$

$$E_{VB} = E_{CB} + E_{g}$$

Here, X is the electronegativity, E_{CB} and E_{VB} are the conduction band and valence band potentials, respectively, E^{c} is equal to 4.5 eV (energy of a free electron at the H_2 scale), and E_g is the calculated band gap (from the Tauc plot). Based on these equations, a type-II heterojunction was formed between B, F and Z. The calculated conduction and valence band positions were at 0.46, 0.33 and −0.4 eV/NHE and at 2.62, 2.43 and 1.5 eV/NHE for B, F and Z, respectively before the contact (Fig. 9(a)).[11,30,33,45–47]

Cyclic voltammetry analysis is the second method and was also performed in order to calculate the HOMO and LUMO band edges positions and the band gap. The details and graphs are shown in Fig. 9(b) and S6 (ESI†). From the graphs it is clear that pristine $BiVO_4$ (B) shows an E_{HOMO} at 3.2 eV and an E_{LUMO}

at 5.4 eV, Fe_2O_3 (F) shows an E_{HOMO} at 3.14 eV and an E_{LUMO} at 5.2 eV and $ZnFe_2O_4$ (Z) shows an E_{HOMO} at 3.0 eV and an E_{LUMO} at 5.09 eV. The estimated band gap values for B, F and Z turn out to be 2.2 eV, 2.06 eV and 2.09 eV, respectively, which match well with the literature reported values. This shows that the sample exhibited a type-II heterojunction formation, which facilitates the charge transfer kinetics at the interface. Thus, the photogenerated electrons present in the conduction band of Z quickly move to F, then to B and then *via* an external circuit reach the Pt electrode, where reduction reaction takes place. Simultaneously, holes present in the valence band of B participate in the oxidation reaction and get transferred to F and then to Z, where oxidation takes place. Thus, band bending due to the appropriate band alignment would smoothen the transport of photogenerated charge carriers across the interface.[48,49]

4. Conclusion of the study

In the present work, we have successfully designed a n/n/n triple heterojunction photoanode consisting of Zr:W-$BiVO_4$, Fe_2O_3, and $ZnFe_2O_4$ as a semiconductor metal oxide fabricated through a spray pyrolysis method. The additions of Zr and W dopants in $BiVO_4$ increases the charge carrier density and reduces their recombination, respectively. Further, Fe_2O_3 and $ZnFe_2O_4$ act as a protective layer for Zr:W-$BiVO_4$, which augments the PEC performance with a 1.90% conversion efficiency. The present study confirms that the so formed triple heterojunction not only suppresses charge recombination but also advances the water oxidation kinetics due to a better separation of the photogenerated charge carriers at the interface of the heterojunction. In addition to this, the triple heterojunction has an extended visible light absorption and maximum donor density.

Author contributions

Sakshi Saxena: conception, methodology, data curation, formal analysis investigation of data, writing-original draft; Anuradha Verma: writing-review and editing, validation, visualization; Kumari Asha: validation and resources; Neeraj Kumar Biswas: validation and resources; Anupam Srivastav: formal analysis and investigation; Vibha Rani Satsangi: conceptualization, visualization; Rohit Shrivastav: conceptualization, visualization; Sahab Dass: writing-review and editing, visualization, supervision, project administration, funding acquisition.

Conflicts of interest

There are no conflicts to declare.

Acknowledgements

Sakshi Saxena thanks the MNRE project (File No. 103/241/2015-NT), Department of Science & Technology, Ministry of Science & Technology, Govt. of India, for an Inspire Fellowship. The authors would like to thank Mr Dev Datt Pal for helping with the XPS analysis and Mr Shyamprasad Mokkapati for doing FESEM analysis.

References

1 **https://www.ics-hydrogen.com**.
2 C. Liu, H. Luo, Y. Xu, Z. Zhang, Q. Liang, W. Wang and Z. Chen, Synergistic cocatalytic effect of ultra-thin metal–organic framework and Mo-dopant for efficient photoelectrochemical water oxidation on $BiVO_4$ photoanode, *Chem. Eng. J.*, 2020, **384**, 123333.
3 A. Eftekhari, V. J. Babu and S. Ramakrishna, Photoelectrode nanomaterials for photoelectrochemical water splitting, *Int. J. Hydrogen Energy*, 2017, **42**(16), 11078–11109.
4 P. M. Pataniya, V. Patel and C. K. Sumesh, Electrophoretic Deposition of $MoSe_2$–MoO_x Nanosheets for Enhanced Electrocatalytic Hydrogen Evolution Reaction, *ACS Appl. Energy Mater.*, 2021, **4**(8), 7891–7899.
5 D. K. Lee, D. Lee, M. A. Lumley and K. S. Choi, Progress on ternary oxide-based photoanodes for use in photoelectrochemical cells for solar water splitting, *Chem. Soc. Rev.*, 2019, **48**(7), 2126–2157.
6 X. Zhao and Z. Chen, Enhanced photoelectrochemical water splitting performance using morphology-controlled $BiVO_4$ with W doping, *Beilstein J. Nanotechnol.*, 2017, **8**(1), 2640–2647.
7 J. Li, J. Li, H. Yuan, W. Zhang, Z. Jiao and X. S. Zhao, Modification of $BiVO_4$ with partially covered α-Fe_2O_3 spindles serving as hole-transport channels for significantly improved photoelectrochemical performance, *Chem. Eng. J.*, 2020, **398**, 125662.
8 R. Shen, L. Zhang, X. Chen, M. Jaroniec, N. Li and X. Li, Integrating 2D/2D CdS/α-Fe_2O_3 ultrathin bilayer Z-scheme heterojunction with metallic β-NiS nanosheet-based ohmic-junction for efficient photocatalytic H_2 evolution, *Appl. Catal., B*, 2020, **266**, 118619.
9 S. M. Tao and L. Y. Lin, Design of efficient Mn-doped α-Fe_2O_3/Ti-doped α-Fe_2O_3 homojunction for catalyzing photoelectrochemical water splitting, *Int. J. Hydrogen Energy*, 2020, **45**(11), 6487–6499.
10 A. Banerjee, B. Mondal, A. Verma, V. R. Satsangi, R. Shrivastav, A. Dey and S. Dass, Enhancing efficiency of Fe_2O_3 for robust and proficient solar water splitting using a highly dispersed bioinspired catalyst, *J. Catal.*, 2017, **352**, 83–92.
11 A. Verma, A. Srivastav, S. A. Khan, V. R. Satsangi, R. Shrivastav, D. K. Avasthi and S. Dass, Enhanced photoelectrochemical response of plasmonic Au embedded $BiVO_4$/Fe_2O_3 heterojunction, *Phys. Chem. Chem. Phys.*, 2017, **19**(23), 15039–15049.
12 K. Asha, V. R. Satsangi, R. Shrivastav, R. Kant and S. Dass, Effect of morphology and impact of the electrode/electrolyte interface on the PEC response of Fe_2O_3 based systems – comparison of two preparation techniques, *RSC Adv.*, 2020, **10**(69), 42256–42266.
13 O. M. Lemine, M. Bououdina, M. Sajieddine, A. M. Al-Saie, M. Shafi, A. Khatab, M. Al-Hilali and M. Henini, Synthesis,

structural, magnetic and optical properties of nanocrystalline $ZnFe_2O_4$, *Phys. B*, 2011, **406**(10), 1989–1994.

14 M. L. Baynosa, A. H. Mady, D. R. Kumar, M. S. Sayed, D. Tuma and J. J. Shim, Eco-friendly synthesis of recyclable mesoporous zinc ferrite@reduced graphene oxide nanocomposite for efficient photocatalytic dye degradation under solar radiation, *J. Colloid Interface Sci.*, 2020, **561**, 459–469.

15 J. Wang, Q. Zhang, F. Deng, X. Luo and D. D. Dionysiou, Rapid toxicity elimination of organic pollutants by the photocatalysis of environment-friendly and magnetically recoverable step-scheme $SnFe_2O_4/ZnFe_2O_4$ nano-heterojunctions, *Chem. Eng. J.*, 2020, **379**, 122264.

16 L. Kong, Z. Jiang, T. Xiao, L. Lu, M. O. Jones and P. P. Edwards, Exceptional visible-light-driven photocatalytic activity over BiOBr–$ZnFe_2O_4$ heterojunctions, *Chem. Commun.*, 2011, **47**(19), 5512–5514.

17 N. Guijarro, P. Bornoz, M. Prévot, X. Yu, X. Zhu, M. Johnson, X. Jeanbourquin, F. Le Formal and K. Sivula, Evaluating spinel ferrites MFe_2O_4 (M = Cu, Mg, Zn) as photoanodes for solar water oxidation: prospects and limitations, *Sustainable Energy Fuels*, 2018, **2**(1), 103–117.

18 D. H. Taffa, R. Dillert, A. C. Ulpe, K. C. Bauerfeind, T. Bredow, D. W. Bahnemann and M. Wark, Photoelectrochemical and theoretical investigations of spinel type ferrites ($M_xFe_{3-x}O_4$) for water splitting: a mini-review, *J. Photonics Energy*, 2016, **7**(1), 012009.

19 L. C. Sonia, M. Victory and S. Phanjoubam, A Comparative Study of the Properties of Zinc Ferrite Nanoparticles Synthesized by Different Techniques for Nanofluid Preparation, *Integr. Ferroelectr.*, 2020, **204**(1), 100–111.

20 J. S. Ma, L. Y. Lin and Y. S. Chen, Facile solid-state synthesis for producing molybdenum and tungsten co-doped monoclinic $BiVO_4$ as the photocatalyst for photoelectrochemical water oxidation, *Int. J. Hydrogen Energy*, 2019, **44**(16), 7905–7914.

21 S. Cao, X. Yan, Z. Kang, Q. Liang, X. Liao and Y. Zhang, Band alignment engineering for improved performance and stability of $ZnFe_2O_4$ modified CdS/ZnO nanostructured photoanode for PEC water splitting, *Nano Energy*, 2016, **24**, 25–31.

22 A. Irshad and N. Munichandraiah, Photochemical deposition of Co-Ac catalyst on ZnO nanorods for solar water oxidation, *J. Electrochem. Soc.*, 2015, **162**(4), H235.

23 A. Verma, A. Srivastav, S. Sharma, P. Badami, V. R. Satsangi, R. Shrivastav, A. M. Kannan, D. K. Avasthi and S. Dass, MWCNTs and Cu_2O sensitized $TiFe_2O_3$ photoanode for improved water splitting performance, *Int. J. Hydrogen Energy*, 2018, **43**(12), 6049–6059.

24 C. Miao, S. Ji, G. Xu, G. Liu, L. Zhang and C. Ye, Micro-nano-structured Fe_2O_3:Ti/$ZnFe_2O_4$ heterojunction films for water oxidation, *ACS Appl. Mater. Interfaces*, 2012, **4**(8), 4428–4433.

25 K. J. McDonald and K. S. Choi, Synthesis and photoelectrochemical properties of $Fe_2O_3/ZnFe_2O_4$ composite photoanodes for use in solar water oxidation, *Chem. Mater.*, 2011, **23**(21), 4863–4869.

26 Y. L. Li, Y. Liu, Y. J. Hao, X. J. Wang, R. H. Liu and F. T. Li, Fabrication of core–shell $BiVO_4$@Fe_2O_3 heterojunctions for realizing photocatalytic hydrogen evolution via conduction band elevation, *Mater. Des.*, 2020, **187**, 108379.

27 A. Srivastav, P. Kumar, A. Verma, Y. R. Smith, V. R. Satsangi, R. Shrivastav, U. V. Waghmare and S. Dass, Experimental and first-principles studies of $BiVO_4/BiV_{1-x}Mn_xO_{4-y}$ n–n^+ homojunction for efficient charge carrier separation in sunlight induced water splitting, *Int. J. Hydrogen Energy*, 2018, **43**(33), 15815–15822.

28 S. A. Salman, N. A. Bakr and R. K. Ismail, Study of the effect of annealing on optical properties of $ZnFe_2O_4$ films prepared by chemical spray pyrolysis method, *International Journal of Thin Film Science and Technology*, 2016, **5**(1), 33–37.

29 S. Saxena, A. Verma, N. K. Biswas, S. A. Khan, V. R. Satsangi, R. Shrivastav and S. Dass, Zr–W Co-doping in $BiVO_4$ – Synergistic effect in photoelectrochemical water splitting, *Mater. Chem. Phys.*, 2021, **267**, 124675.

30 G. Kaur, S. A. Khan, V. R. Satsangi, S. Dass and R. Shrivastav, Nano-hetero-structured thin films, ZnO/Ag-(α)Fe_2O_3, with n/n junction, as efficient photoanode for renewable hydrogen generation via photoelectrochemical water splitting, *Renewable Energy*, 2021, **164**, 156–170.

31 J. Li, J. Li, H. Yuan, W. Zhang, Z. Jiao and X. S. Zhao, Modification of $BiVO_4$ with partially covered α-Fe_2O_3 spindles serving as hole-transport channels for significantly improved photoelectrochemical performance, *Chem. Eng. J.*, 2020, **398**, 125662.

32 X. Wang, J. Feng, Z. Zhang, W. Zeng, M. Gao, Y. Lv, T. Wei, Y. Ren and Z. Fan, Pt enhanced the photo-Fenton activity of $ZnFe_2O_4$/α-Fe_2O_3 heterostructure synthesized via one-step hydrothermal method, *J. Colloid Interface Sci.*, 2020, **561**, 793–800.

33 X. Xu and W. Song, Synthesis and photocatalytic activity of heterojunction $ZnFe_2O_4$–$BiVO_4$, *Materials Technology*, 2017, **32**(8), 472–479.

34 P. Kumar, P. Sharma, R. Shrivastav, S. Dass and V. R. Satsangi, Electrodeposited zirconium-doped α-Fe_2O_3 thin film for photoelectrochemical water splitting, *Int. J. Hydrogen Energy*, 2011, **36**(4), 2777–2784.

35 K. Uma, B. KrishnaKumar, G. T. Pan, T. C. Yang and J. H. Lin, Enriched silver plasmon resonance activity on the sonochemical synthesis of ZnO flowers with α-Fe_2O_3 as an efficient catalyst for photo-Fenton reaction and photo-oxidation of ethanol, *Journal of Water Process Engineering*, 2020, **34**, 101089.

36 A. A. Tahir and K. U. Wijayantha, Photoelectrochemical water splitting at nanostructured $ZnFe_2O_4$ electrodes, *J. Photochem. Photobiol., A*, 2010, **216**(2–3), 119–125.

37 M. Wang, Y. Sun, H. Chen, Y. Zhang, X. Wu, K. Huang and S. Feng, Enhanced photoelectrochemical activity of nanostructured $ZnFe_2O_4$ thin films prepared by the electrospray technique, *CrystEngComm*, 2017, **19**(5), 772–775.

38 Y. Guo, Y. Fu, Y. Liu and S. Shen, Photoelectrochemical activity of $ZnFe_2O_4$ modified α-Fe_2O_3 nanorod array films, *RSC Adv.*, 2014, **4**(70), 36967–36972.

39 R. Appiah-Ntiamoah, A. F. Baye and H. Kim, In Situ Electrochemical Formation of a Core–Shell $ZnFe_2O_4$@Zn(Fe)OOH Heterostructural Catalyst for Efficient Water Oxidation in Alkaline Medium, *ChemElectroChem*, 2020, **7**(16), 3478–3486.

40 M. Chakraborty, D. Roy, A. Sharma and R. Thangavel, Post-treatment with $ZnFe_2O_4$ nanoparticles to improve photo-electrochemical performance of ZnO nanorods based photoelectrodes, *Sol. Energy Mater. Sol. Cells*, 2019, **200**, 109975.

41 K. Asha, A. Banerjee, S. Saxena, S. A. Khan, I. Sulaniya, V. R. Satsangi, R. Shrivastav, R. Kant and S. Dass, Morphological influence of electrode/electrolyte interface towards augmenting the efficiency of photoelectrochemical water splitting – A case study on ZnO, *J. Power Sources*, 2019, **432**, 38–47.

42 S. S. Bhat, S. A. Lee, J. M. Suh, S. P. Hong and H. W. Jang, Triple planar heterojunction of SnO_2/WO_3/$BiVO_4$ with enhanced photoelectrochemical performance under front illumination, *Appl. Sci.*, 2018, **8**(10), 1765.

43 N. A. Mohamed, J. Safaei, A. F. Ismail, M. N. Khalid, M. F. Jailani, M. F. Noh, N. A. Arzaee, D. Zhou, J. S. Sagu and M. A. Teridi, Boosting photocatalytic activities of $BiVO_4$ by creation of g-C_3N_4/ZnO@$BiVO_4$ heterojunction, *Mater. Res. Bull.*, 2020, **125**, 110779.

44 S. Bai, J. Han, K. Zhang, J. Sun, J. Guo, R. Luo, D. Li and A. Chen, Triadic layered double hydroxide modified semiconductor heterojunction for PEC water splitting, *ACS Sustainable Chem. Eng.*, 2020, **8**(10), 4076–4084.

45 T. W. Kim and K. S. Choi, Improving stability and photoelectrochemical performance of $BiVO_4$ photoanodes in basic media by adding a $ZnFe_2O_4$ layer, *J. Phys. Chem. Lett.*, 2016, **7**(3), 447–451.

46 T. B. Nguyen and R. A. Doong, Heterostructured $ZnFe_2O_4$/TiO_2 nanocomposites with a highly recyclable visible-light-response for bisphenol A degradation, *RSC Adv.*, 2017, **7**(79), 50006–50016.

47 K. Xiong, K. Wang, L. Chen, X. Wang, Q. Fan, J. Courtois, Y. Liu, X. Tuo and M. Yan, Heterostructured $ZnFe_2O_4$/Fe_2TiO_5/TiO_2 Composite Nanotube Arrays with an Improved Photocatalysis Degradation Efficiency Under Simulated Sunlight Irradiation, *Nano-Micro Lett.*, 2018, **10**(1), 17.

48 A. Shafiee, M. M. Salleh and M. Yahaya, Determination of HOMO and LUMO of [6,6]-phenyl C61-butyric acid 3-ethylthiophene ester and poly(3-octyl-thiophene-2,5-diyl) through voltammetry characterization, *Sains Malays.*, 2011, **40**(2), 173–176.

49 L. Leonat, G. Sbarcea and I. V. Branzoi, Cyclic voltammetry for energy levels estimation of organic materials, *UPB Scientific Bulletin, Series B: Chemistry and Materials Science*, 2013, **75**(3), 111–118.